

A Ni-based Superconductor: the Heusler Compound ZrNi₂Ga.

Jürgen Winterlik, Gerhard H. Fecher and Claudia Felser*

Institut für Anorganische und Analytische Chemie,

Johannes Gutenberg - Universität, 55099 Mainz, Germany.

Martin Jourdan

Institut für Physik, Johannes Gutenberg - Universität, 55128 Mainz, Germany.

Kai Grube

Forschungszentrum Karlsruhe, Institut für Festkörperphysik,

P.O. Box 3640, 76021 Karlsruhe, Germany

Frédéric Hardy and Hilbert von Löhneysen

Forschungszentrum Karlsruhe, Institut für Festkörperphysik,

P.O. Box 3640, 76021 Karlsruhe, Germany, and Physikalisches Institut,

Universität Karlsruhe, 76128 Karlsruhe, Germany

K. L. Holman and R. J. Cava

Department of Chemistry, Princeton University,

Princeton, New Jersey 08544, USA

(Dated: November 3, 2018)

Abstract

This work reports on the novel Heusler superconductor ZrNi_2Ga . Compared to other nickel-based superconductors with Heusler structure, ZrNi_2Ga exhibits a relatively high superconducting transition temperature of $T_c = 2.9$ K and an upper critical field of $\mu_0 H_{c2} = 1.5$ T. Electronic structure calculations show that this relatively high T_c is caused by a van Hove singularity, which leads to an enhanced density of states at the Fermi energy $N(\epsilon_F)$. The van Hove singularity originates from a higher order valence instability at the L -point in the electronic structure. The enhanced $N(\epsilon_F)$ was confirmed by specific heat and susceptibility measurements. Although many Heusler compounds are ferromagnetic, our measurements of ZrNi_2Ga indicate a paramagnetic state above T_c and could not reveal any traces of magnetic order down to temperatures of at least 0.35 K. We investigated in detail the superconducting state with specific heat, magnetization, and resistivity measurements. The resulting data show the typical behavior of a conventional, weakly coupled BCS (s-wave) superconductor.

PACS numbers: 71.20.Be, 74.70.Ad, 75.20.En, 85.25.Cp

Keywords: Superconductivity, Electronic structure, Heusler compounds

I. INTRODUCTION

In the research area of spintronics applications, Heusler compounds have become of interest as half-metals, where due to the exchange splitting of the d -electron states, only electrons of one spin direction have a finite density of states at the Fermi level $N(\epsilon_F)^{1,2}$. Up to the present, very few Heusler superconductors with the ideal formula of AB_2C have been found. In 1982, the first Heusler superconductors were reported, each with a rare-earth metal in the B position³. Among the Heusler superconductors, Pd-based compounds have attracted attention because YPd_2Sn exhibits the highest yet recorded T_c of 4.9 K⁴. Moreover, coexistence of superconductivity and antiferromagnetic order was found in $YbPd_2Sn$ ⁵ and $ErPd_2Sn$ ⁶. A systematic investigation of Ni-based Heusler compounds seems to be worthwhile as nickel has many properties in common with palladium but tends more towards magnetic order due to the smaller hybridization of the $3d$ -states. In fact, elementary nickel is a ferromagnet. Thus, nickel-containing Heusler compounds with a high proportion of Ni are naively expected to show magnetic order rather than superconductivity. However, superconductivity of Ni-rich alloys $NbNi_2C$ ($C = Al, Ga, Sn$) has been reported some time ago, with transition temperatures T_c ranging from 1.54 K to the highest recorded transition temperature of a Ni-based Heusler compound of 3.4 K in $NbNi_2Sn$ ^{4,7}. In contrast to the two aforementioned Pd-based compounds these superconductors do not show indications of magnetic order. Currently there is a lot of excitement about the new high temperature superconductors based on FeAs⁸. The superconductivity of these compounds is related to two-dimensional layers of edge shared FeAs tetrahedrons⁹. These structure types can be understood as two-dimensional variants of the Heusler structure.

A clear understanding of the origin of superconductivity, magnetism, and their possible coexistence in Heusler compounds is still missing. To shed light on the relation between the electronic structure and the resulting ground state of AB_2C Heusler compounds we searched for new Ni-based Heusler compounds with a high density of states (DOS) at ϵ_F close to the Stoner criterion for ferromagnetism. A possible route for increasing $N(\epsilon_F)$ is the use of saddle points in the energy dispersion curves of the electronic structure. They lead to maxima in the DOS, so-called van Hove singularities¹⁰. In order to identify such compounds, we have performed electronic structure calculations using *ab initio* methods. In a simple approach following the Bardeen-Cooper-Schrieffer theory (BCS) and neglecting any magnetic order, we

would expect that the superconducting transition temperature of such compounds increases with $N(\epsilon_F)$ according to $T_c \approx \Theta_D \exp(-1/V_0 N(\epsilon_F))$ if the Debye temperature Θ_D and the Cooper-pairing interaction V_0 are independent of $N(\epsilon_F)$. In fact, this van Hove scenario, where a maximum in the DOS is ideally located at ϵ_F , was used to explain the unusually high transition temperatures of the intermetallic A15 superconductors¹¹. The correspondence between T_c and the valence electron count is known as Matthias rule¹². According to this rule, the high T_c of the A15 compounds was related to electron concentrations of about 4.6 and 6.4 electrons per atom, leading to a maximum of the DOS at ϵ_F ¹³.

On the basis of the van Hove scenario, we already found superconductivity in two Heusler compounds with 27 electrons: ZrPd₂Al and HfPd₂Al^{14,15}. Here, we report on the theoretical and experimental characterization of the new, Ni-containing, superconducting Heusler compound ZrNi₂Ga. Additionally, electron-doped alloys Zr_{1-x}Nb_xNi₂Ga were prepared and investigated to obtain information about the dependence of T_c on the location of the van Hove singularity.

II. EXPERIMENTAL DETAILS

Polycrystalline ingots of ZrNi₂Ga and electron-doped alloys Zr_{1-x}Nb_xNi₂Ga were prepared by repeated arc melting of stoichiometric mixtures of the corresponding elements in an argon atmosphere at a pressure of 10^{-4} mbar. Care was taken to avoid oxygen contamination. The samples were annealed afterward for 2 weeks at 1073 K in an evacuated quartz tube. After the annealing process, the samples were quenched in a mixture of ice and water to retain the desired $L2_1$ structure. The crystal structure of ZrNi₂Ga was investigated using powder X-ray diffraction (XRD). The measurements were carried out using a Siemens D5000 with monochromatized Cu K_α radiation.

The electrical resistance of a bar shaped sample was measured using a four-point probe technique. The magnetization measurements below a temperature of 4 K were performed in a superconducting quantum interference device (SQUID, Quantum Design MPMS-XL-5). For higher temperatures, the magnetization was measured using a vibrating sample magnetometer (VSM option of a Quantum Design PPMS). The measured samples had a spherical shape with a mass of approximately 20 mg to 120 mg. In order to study the diamagnetic shielding, the sample was initially cooled down to $T = 1.8$ K without applying

any magnetic field, i.e., zero-field cooled (ZFC). Then a field of $\mu_0 H = 2.5$ mT was applied, and the sample magnetization was recorded with increasing temperature. To determine the Meissner effect (flux expulsion) the sample was subsequently cooled and its magnetization measured in the identical field, i.e., field cooled (FC). The field dependent magnetization of ZrNi₂Ga was measured at a temperature of 2 K. Finally, the normal-state susceptibility was measured at $\mu_0 H = 2$ T in a temperature range from 1.8 K to 300 K. Specific-heat measurements were carried out at $0.35 \text{ K} < T < 4 \text{ K}$ in magnetic fields of up to 5 T in a Quantum Design PPMS with a ³He option.

III. *AB INITIO* CALCULATIONS OF THE ELECTRONIC AND VIBRATIONAL PROPERTIES.

The electronic and vibrational properties were calculated through the use of WIEN2k¹⁶ in combination with PHONON¹⁷. The electronic structure of ZrNi₂Ga was calculated by means of the full potential linearized augmented plane wave (FLAPW) method as implemented in WIEN2k provided by Blaha, Schwartz, and coworkers^{16,18,19}. The exchange-correlation functional was taken within the generalized gradient approximation (GGA) in the parameterization of Perdew, Burke and Enzerhof²⁰. A $25 \times 25 \times 25$ point mesh was used as base for the integration in the cubic systems resulting in 455 k -points in the irreducible wedge of the Brillouin zone. The energy convergence criterion was set to 10^{-5} Ry and simultaneously the criterion for charge convergence to $10^{-3}e^-$. The muffin tin radii were set to $2.5 a_{0B}$ ($a_{0B} :=$ Bohr's radius) for the transition metals as well as the main group element. A volume optimization resulted in $a_{opt} = 6.14 \text{ \AA}$ and a bulk modulus of $B = 156 \text{ GPa}$ for the relaxed structure. This value is slightly larger than the experimentally observed lattice parameter a_{exp} (see below). The results presented in the following are for the relaxed lattice parameter, no noticeable changes are observed in the calculations using a_{exp} .

Figure 1 shows the results for the electronic structure from the *ab initio* calculations. Typical for Heusler compounds is the low lying hybridization gap at energies between 7 eV and 5.6 eV below the Fermi energy. This gap emerges from the strong interaction of the $s-p$ states at the Ga atoms in O_h symmetry with the eight surrounding Ni atoms. It explains the structural stability of the compound.

More interesting are the bands close to the Fermi energy. In particular, the topmost

valence band exhibits a van Hove singularity at the L -point only 70 meV above ϵ_F . The result is a maximum of the density of states at the Fermi energy (see Figure 1(b)). A closer inspection of those states reveals that the singularity at L is a S_2 -type saddle point of the electronic structure with a twofold degeneracy. This degeneracy is removed along LK or LW . For both bands, two of the second derivatives $|\partial^2 E(k)/\partial k_i \partial k_j|_{k_e}$ of the dispersion $E(k)$ are > 0 and one is < 0 (Λ -direction) at $k_e = (1/4, 1/4, 1/4)$.

Figure 2 shows the calculated phonon dispersion and phonon density of states. The dispersion of the acoustic LA and TA_1 modes is degenerate in the fourfold Δ direction as well as along Λ . This degeneracy is removed at the K -point and in the twofold Σ direction. Instabilities in the form of soft-phonon modes, as are observed for several magnetic Ni-based Heusler compounds^{21,22}, do not occur in the phonon dispersion relation of $ZrNi_2Ga$. This indicates the high structural stability of the compound compared to the Ni-based Heusler shape memory alloys (for example Ni_2MnGa).

The high density of phonons at energies of about 30 meV is due to the vibration of the rather heavy Zr atoms. These optical modes have no overlap with the remainder of the phonon spectrum and appear as Einstein frequencies. In a hybrid Einstein-Debye model, this corresponds to an Einstein temperature of $\Theta_E \approx 340$ K and a Debye temperature of $\Theta_D \approx 270$ K taken from the density maximum at the upper cut-off of the optical modes.

IV. RESULTS AND DISCUSSION

A. Crystal structure and sample quality

$ZrNi_2Ga$ crystallizes in the cubic $L2_1$ Heusler structure (space group: $Fm\bar{3}m$), where the Wyckoff positions are $4a$ (0,0,0) for Zr atoms, $4b$ ($\frac{1}{2}, \frac{1}{2}, \frac{1}{2}$) for Ga atoms, and $8c$ ($\frac{1}{4}, \frac{1}{4}, \frac{1}{4}$) for Ni atoms. Figure 3 shows the diffraction pattern for $ZrNi_2Ga$ with the raw data above (black) and the difference between a calculated Rietveld-refinement and the raw data below (grey). Within the experimental resolution of the diffractometer, no secondary phases were observed. The Rietveld refinement results in a cubic lattice parameter of $a = 6.098 \pm 0.003$ Å. The as-cast samples of $ZrNi_2Ga$ were indistinguishable from the annealed ones in their XRD patterns, but magnetic, transport, and specific-heat measurements suggested an improved quality of the annealed samples. This improved quality of the annealed crystals was con-

firmly by resistivity measurements yielding a residual resistivity ratio of two, which is typical for polycrystalline Heusler compounds. The specific-heat and magnetization measurements reveal sharp superconducting transitions of $\Delta T_c/T_c \leq 0.03$. At low temperature, however, the measurements indicate small sample inhomogeneities or impurities.

B. Properties of the superconducting state

The superconducting transition of ZrNi₂Ga was observed in measurements of the electrical resistance. Figure 4 displays the temperature dependence of the resistance, which exhibits metallic behavior and a transition to superconductivity at $T_c = 2.87 \pm 0.03$ K.

Magnetization measurements using SQUID magnetometry were carried out to confirm bulk superconductivity in ZrNi₂Ga. The results of the magnetization measurements are given in Figure 5. The upper panel (a) shows the temperature dependent magnetization $M(T)$ of a nearly spherical sample in an external field of $\mu_0 H = 2.5$ mT. A sharp onset of superconductivity is observed in the ZFC curve at a temperature of $T_c = 2.80$ K. The sharpness of the transition indicates good sample quality. The resistive transition appears at a slightly higher temperature than that determined from the magnetization measurements. This is a well known phenomenon: the resistive transition occurs when one percolation path through the sample becomes superconducting whereas the magnetic transition requires a certain superconducting volume. The ZFC curve demonstrates complete diamagnetic shielding. For the calculation of the magnetic volume susceptibility, we used the demagnetization factor $\frac{1}{3}$ of a sphere. The deviation from the expected value of -1 (100% shielding) is ascribed to an imperfect spherical shape of the sample and therefore an underestimated demagnetization factor. The FC curve represents the Meissner effect for superconducting ZrNi₂Ga. The large difference between the ZFC and the FC curves shows clearly that ZrNi₂Ga is a type-II superconductor and points to a weak Meissner effect due to strong flux pinning. Figure 5(b) shows a plot of the field dependent magnetization (M - H curve). The magnetic field was varied from -100 mT to 100 mT at a constant temperature of 2 K. The $M(H)$ measurements exhibit the typical butterfly loop of an irreversible type-II superconductor with large hysteresis due to strong flux pinning. An accurate determination of the lower critical magnetic field H_{c1} at this temperature is nearly not possible because of the broadening of the $M(H)$ curves. A very rough estimation of H_{c1} , defined as the magnetic field

where the initial slope intersects with the extrapolation curve of $(M_{up} + M_{down})/2$, yields $\mu_0 H_{c1}(T = 2 \text{ K})$ of approximately 16 mT compared to the upper critical field at $T = 2 \text{ K}$ of 0.62 T.

Figure 6 shows the electronic contribution to the specific heat C_e of ZrNi₂Ga plotted as C_e/T vs. T in various magnetic fields. The phonon contribution to the specific heat was subtracted as will be shown below. The main feature of C_e/T is the specific-heat jump ΔC_e at $T_c = 2.83 \text{ K}$ with a width of 0.1 K. The nearly perfect agreement between the differently determined T_c values together with the large ΔC_e confirm bulk superconductivity in ZrNi₂Ga. An analysis of the jump yields $\Delta C_e/\gamma_n T_c = 1.41$, which is in very good agreement with the weak-coupling BCS value of 1.43. Here γ_n denotes the normal-state Sommerfeld coefficient, which is discussed below. The energy gap is obtained from a plot of $C_e/\gamma T_c$ on a logarithmic scale versus T_c/T , as shown in Figure 7. A comparison with the BCS formula for C_e well below T_c

$$C_e/\gamma T_c = 8.5 \exp[-(0.82\Delta(0)/k_B T)]$$

yields an energy gap $\Delta(0)$ of 0.434 meV for $T \rightarrow 0$ and $2\Delta(0)/k_B T_c = 3.53$, again in very good agreement with the weak-coupling BCS value. At lowest temperatures one can observe deviations from the expected behavior. As these deviations are sample dependent and clearly reduced in the annealed samples we attribute them to the aforementioned sample imperfections. In a more detailed analysis we compared C_e at zero field with the calculated behavior of a BCS superconductor by using the approach of Padamsee *et al.*²³ and the temperature dependence of the gap $\Delta(T)$ of Mühlischlegel²⁴. In this model, C_e is estimated for a system of independent fermion quasiparticles with

$$\frac{S}{\gamma_n T_c} = -\frac{6}{\pi^2} \frac{\Delta(0)}{k_B T_c} \int_0^\infty [f \ln f + (1-f) \ln(1-f)] dy,$$

$$\frac{C_e}{\gamma_n T_c} = t \frac{\partial(S/\gamma_n T_c)}{\partial t}$$

where

$$f = [\exp(\sqrt{\epsilon^2 + \Delta^2(t)}/k_B T + 1)], \quad t = T/T_c, \quad y = \epsilon/\Delta_0.$$

The only free parameter, the ratio $2\Delta(0)/k_B T_c$, was set to 3.53. Indeed, the specific heat can overall be rather well described by the weak-coupling BCS theory, as can be seen in Figure 6. To study the influence of the magnetic field we plot C_e/T at a constant temperature of 0.5 K

vs. the H/H_{c2} in the inset of Figure 7. The linear increase of C_e/T with H corresponds to an isotropic gap, as expected for a cubic BCS superconductor.

Further $R(T)$ measurements in various magnetic fields were performed to determine the upper critical field H_{c2} of ZrNi₂Ga. In Figure 8 the data are summarized together with those of the specific-heat measurements. $H_{c2}(T)$ was theoretically derived by Wertheimer, Helfland, and Hohenberg (WHH)²⁵ in the limit of short electronic mean free path (dirty limit), including, apart from the usual orbital pair breaking, the effects of Pauli spin paramagnetism and spin-orbit scattering. The model has two adjustable parameters: the Maki parameter α , which represents the limitation of H_{c2} by the Pauli paramagnetism, and the spin-orbit scattering constant λ_{so} . α can be determined from the initial slope of the upper critical field

$$\alpha = -0.53 \cdot \mu_0 \left. \frac{dH_{c2}}{dT} \right|_{T=T_c} (\mu_0 H \text{ in T}),$$

or via the Sommerfeld coefficient γ_n and the residual resistivity ρ_0 with:

$$\alpha = 2e^2 \hbar \gamma_n \rho_0 / (2\pi^2 m k_B^2),$$

where m and e are the free electron mass and charge, respectively. From the data we extract $\mu_0 \left. \frac{dH_{c2}}{dT} \right|_{T=T_c} = -0.75$ T/K and $\alpha = 0.4$. With $\lambda_{so} \rightarrow \infty$, the curve estimated by the WHH model follows the data points very closely, as is seen in Figure 8. As the spin-orbit scattering counteracts the effect of the Pauli paramagnetism, this is equal to $\alpha = 0$ and $\lambda_{so} = 0$, representing the upper bound of H_{c2} where pair breaking is only induced by orbital fields. Consequently, the temperature dependence of H_{c2} can either be explained by Pauli paramagnetism with an extremely strong spin-orbit scattering or with a dominating orbital field effect. The critical field due to the Pauli term alone is $\mu_0 H_p(0) = \mu_0 \Delta(0) / \sqrt{2} \mu_B = 1.84 T_c = 5.24$ T, which is much higher than H_{c2} in the absence of Pauli paramagnetism $\mu_0 H_{c2}^*(0) = -0.69 \cdot \mu_0 \left. \frac{dH_{c2}}{dT} \right|_{T=T_c} = 1.48$ T. Hence pair breaking in ZrNi₂Ga is most probably only caused by orbital fields²⁶. This is in contrast to other Ni-based Heusler superconductors like Ni₂NbGa and Ni₂NbSn where $H_{c2}^*(0)$ is clearly larger than the measured critical fields and therefore the Pauli paramagnetic effect has to be considered (see Table I).

The thermodynamic critical field was calculated from the difference between the free

energy of the superconducting and the normal states:

$$\mu_0 H_c = \left[2\mu_0 \int_{T_c}^T \int_{T_c}^T (C_e/T'' - \gamma_n) dT'' dT' \right]^{\frac{1}{2}}.$$

A value of $\mu_0 H_c = 44.6$ mT is obtained. From the upper and thermodynamic critical field one can estimate the Ginzburg-Landau parameter κ_{GL} , which is the ratio of the spatial variation length of the local magnetic field λ_{GL} and the coherence length ξ_{GL} : $\kappa_{GL} = H_{c2}(\sqrt{2}H_c) = \lambda_{GL}/\xi_{GL} = 23.5$. The isotropic Ginsburg-Landau-Abrikosov-Gor'kov theory leads to the values of $\xi_{GL} = \sqrt{\Phi_0/2\pi\mu_0 H_{c2}} = 15$ nm and $\lambda_{GL} = 350$ nm (Φ_0 is the fluxoid quantum $h/2e$).

Obviously, ZrNi₂Ga is a conventional, weakly coupled, fully gapped type-II superconductor that is best described in terms of weak-coupling BCS superconductivity. If a phonon mediated pairing mechanism is assumed, we can determine the dimensionless electron-phonon coupling constant λ by using the McMillan relation²⁷:

$$T_c = \frac{\Theta_D}{1.45} \exp \left[\frac{-1.04(1 + \lambda)}{\lambda - \mu_c^*(1 + 0.62\lambda)} \right].$$

If the Coulomb coupling constant μ_c^* is set to its usual value of 0.13 and Θ_D to our measured value of 300 K we get $\lambda = 0.551$, which is in good accordance with other superconducting Heusler compounds⁷.

C. Normal state properties

Now we turn to a characterization of the normal state properties. When superconductivity is suppressed in a magnetic field of $H > H_{c2}$, the Sommerfeld coefficient γ_n and the Debye temperature Θ_D can be extracted from the low-temperature behavior of the specific heat, $C = \gamma_n T + \frac{12}{5}\pi^4 R n \theta_D^{-1} T^3$ where R is the gas constant and n the number of atoms per formula unit (= 4 in the case of Heusler compounds). The extracted Debye temperature $\Theta_D = 300$ K agrees very well with the calculated value of 270 K and is in the typical Θ_D range of other Heusler compounds (see Table I).

Likewise in accordance to our electronic structure calculations, the high density of states leads to a strongly enhanced Sommerfeld coefficient of $\gamma_n = \frac{\pi^2}{3} k_B^2 N(\epsilon_F) = 17.3$ mJ/mol K². In fact, γ_n is one of the highest values for paramagnetic Ni-based Heusler compounds (see Table I). As already stated by Boff *et al.*²⁸, the maximum of γ_n in the isoelectronic sequence

$A = \text{Ti, Zr, Hf}$ of ANi_2C ($\text{C} = \text{Al, Sn}$) is found for Zr and in the sequence $A = \text{V, Nb, Ta}$ for V. As the electronic structure of all these compounds is quite similar, and consequently a rigid-band model may be applicable, the Fermi level can be shifted through the appropriate choice of A to a maximum of $N(\epsilon_F)^{28,29,30}$. This behavior and the comparatively large γ_n of ZrNi_2Ga confirm the van Hove scenario.

The measured magnetic susceptibility $\chi(T)$ as shown in Figure 9 is nearly independent of T , indicative of a predominantly Pauli-like susceptibility. No sign of magnetic order can be found down to $T = 1.8$ K. Even more, the low-temperature specific-heat measurements demonstrate clearly that apart from the superconductivity no other phase transitions occur down to temperatures of 0.35 K. The enhanced susceptibility corresponds to the high density of states seen in γ_n value as evidenced by the Wilson ratio $R = (\chi/\gamma_n) \cdot \pi^2 k_B^2 / 3\mu_0 \mu_{eff}^2 = 0.97$ where we have set $\mu_{eff}^2 = g^2 \mu_B^2 J(J+1)$ to its free electron values: i.e., the Landé factor $g = 2$ and the total angular momentum $J = \frac{1}{2}$. The resulting Wilson ratio is close to that for independent electrons ($R = 1$).

Below about 10 K, a Curie-Weiss like increase of χ is observed for all samples. A fit of a Curie-Weiss law to the data yields a Weiss temperature of -3.3 K and an effective moment of $0.06 \mu_B/\text{f.u.}$ (assuming $s = 1/2$). This Curie-Weiss like behavior is sample dependent and can again be attributed to a small amount of magnetic impurities. It is, however, supervising that no appreciable pair breaking is observed as evidenced by the validity of the BCS law of corresponding states $2\Delta(0) = 3.53k_B T_c$.

Finally, we want to discuss the influence of the increased DOS on the superconducting properties of ZrNi_2Ga . Although ZrNi_2Ga exhibits an enhanced γ_n compared to the value 5.15 mJ/mol K^2 of NbNi_2Sn , both compounds have nearly the same transition temperature. Obviously, the simple relationship between $N(\epsilon_F)$ and T_c does not hold. Table I demonstrates, likewise, that the upper critical field H_{c2} and the orbital limit H_{c2}^* apparently do not depend on the density of states in these materials.

V. ELECTRON DOPING

The influence of the increased DOS on the superconducting properties is investigated from another point of view, which refers only to ZrNi_2Ga and the van Hove singularity in this compound: the Fermi level can be shifted with an appropriate choice of A , and the

van Hove scenario yields a maximum T_c when the van Hove singularity coincides with ϵ_F . According to the electronic structure calculations, electron-doping of ZrNi_2Ga should lead to this desired coincidence. Therefore, we doped ZrNi_2Ga with electrons in the A position by substituting Zr with distinct amounts of Nb. The alloys $\text{Zr}_{1-x}\text{Nb}_x\text{Ni}_2\text{Ga}$ with $x = 0.15, 0.3, 0.5, \text{ and } 0.7$ were prepared according to Section II.

The crystal structures of the alloys were determined using a Siemens D8 Advance diffractometer with Mo K_α radiation. All alloys were found to crystallize in the Heusler structure (space group: $Fm\bar{3}m$). The atomic radius of Nb is smaller than the one of Zr, and thus a decrease of the lattice parameter is expected upon substituting Zr with Nb. In fact, this effect was observed (Figure 10). No impurity phases were detected in all alloys except of $\text{Zr}_{0.3}\text{Nb}_{0.7}\text{Ni}_2\text{Ga}$. The small difference between the lattice parameters of $\text{Zr}_{0.3}\text{Nb}_{0.7}\text{Ni}_2\text{Ga}$ and $\text{Zr}_{0.5}\text{Nb}_{0.5}\text{Ni}_2\text{Ga}$ supports that a saturation of Nb in the lattice of $\text{Zr}_{1-x}\text{Nb}_x\text{Ni}_2\text{Ga}$ is reached for a value of $0.5 \leq x \leq 0.7$. Increasing the Nb concentration above the saturation limit leads to a segregation of impurities. One of them was identified as elementary Zr.

The superconducting transitions of the alloys were analyzed in magnetization measurements using a SQUID as described in Section II. Figure 11 shows the ZFC curves of the alloys $\text{Zr}_{0.85}\text{Nb}_{0.15}\text{Ni}_2\text{Ga}$, $\text{Zr}_{0.7}\text{Nb}_{0.3}\text{Ni}_2\text{Ga}$, and $\text{Zr}_{0.5}\text{Nb}_{0.5}\text{Ni}_2\text{Ga}$. $\text{Zr}_{0.3}\text{Nb}_{0.7}\text{Ni}_2\text{Ga}$ did not show a superconducting transition down to 1.8 K. This is not surprising because of the impurities, which were detected from XRD in this alloy. The other alloys show a trend of decreasing T_c with increasing Nb concentration as summarized in Table II. It is therefore deduced that the Nb atoms act as additional scattering centres that suppress the bulk superconductivity of ZrNi_2Ga .

VI. CONCLUSIONS

Starting with electronic structure calculations, the Heusler compound ZrNi_2Ga was predicted to have an enhanced density of states at the Fermi energy $N(\epsilon_F)$ due to a van Hove singularity close to ϵ_F . According to the BCS model, ZrNi_2Ga was therefore expected to be an appropriate candidate for superconductivity with a comparatively high superconducting transition temperature.

The predicted superconducting transition was found at $T_c = 2.87$ K. Specific-heat and magnetization measurements proved bulk superconductivity in this material and demon-

strate that ZrNi_2Ga is a conventional, weakly coupled BCS type-II superconductor. The electronic specific heat of the normal state shows a clearly enhanced Sommerfeld coefficient γ_n , which supports the van Hove scenario. In the temperature range $0.35 \text{ K} < T < 300 \text{ K}$, no sign of magnetic order is found. Apparently, the high $N(\epsilon_F)$ is not sufficient to satisfy the Stoner criterion. The normal-state susceptibility is described best by an increased Pauli paramagnetism, corresponding to an enhanced $N(\epsilon_F)$. Despite the presence of magnetic impurities, which would suppress the energy gap by pair breaking, the BCS law of corresponding states holds. This point deserves further investigations.

Acknowledgments

This work is funded by the DFG in Collaborative Research Center "Condensed Matter Systems with Variable Many-Body Interactions" (Transregio SFB/TRR 49). The work at Princeton was supported by the US Department of Energy division of Basic Energy Sciences, grant DE-FG02-98ER45706. The authors would like to thank Gerhard Jakob for many suggestions and for fruitful discussions.

* Electronic address: felser@uni-mainz.de

¹ H. C. Kandpal, G. H. Fecher, and C. Felser, J. Phys. D: Appl. Phys. **40**, 1507 (2007).

² C. Felser, G. H. Fecher, and B. Balke, Angew. Chem. Int. Ed. **46**, 668 (2007).

³ M. Ishikawa, J. L. Jorda, and A. Junod, *Superconductivity in d- and f-band metals 1982* (W. Buckel and W. Weber, Kernforschungszentrum Karlsruhe, Germany, 1982).

⁴ J. H. Wernick, G. W. Hull, J. E. Bernardini, and J. V. Waszczak, Mater. Lett. **2**, 90 (1983).

⁵ H. A. Kierstead, B. D. Dunlap, S. K. Malik, A. M. Umarji, and G. K. Shenoy, Phys. Rev. B **32**, 135 (1985).

⁶ R. N. Shelton, L. S. Hausermann-Berg, M. J. Johnson, P. Klavins, and H. D. Yang, Phys. Rev. B **34**, 199 (1986).

⁷ S. Waki, Y. Yamaguchi, and K. Mitsugi, J. Phys. Soc. Jpn. **54**, 1673 (1985).

⁸ Y. Kamihara, H. Hiramatsu, M. Hirano, R. Kawamura, H. Yanagi, T. Kamiya, and H. Hosono, J. Am. Chem. Soc. **128**, 10012 (2006).

- ⁹ V. Hlukhyya, N. Chumalo, V. Zaremba, and T. F. Fässler, *Z. Anorg. Allg. Chem.* **634**, 1249 (2008).
- ¹⁰ L. van Hove, *Phys. Rev.* **89**, 1189 (1953).
- ¹¹ J. Labbé and J. Friedel, *J. Phys. (Paris)* **27**, 153 (1966).
- ¹² B. T. Matthias, *Phys. Rev.* **92**, 874 (1953).
- ¹³ S. V. Vonsovsky, Y. A. Izyumov, and E. Z. Kurmaev, *Superconductivity of Transition Metals* (Springer-Verlag, Berlin, Heidelberg, 1982).
- ¹⁴ C. Felser, *J. Sol. State Chem.* **160**, 93 (2001).
- ¹⁵ J. Winterlik, G. H. Fecher, and C. Felser, *Solid State Commun.* **145**, 475 (2008).
- ¹⁶ K. Schwarz, P. Blaha, and G. K. H. Madsen, *Comput. Phys. Commun.* **147**, 71 (2002).
- ¹⁷ K. Parlinski, *Software Phonon* (2006).
- ¹⁸ P. Blaha, K. Schwarz, G. K. H. Madsen, D. Kvasnicka, and J. Luitz, *WIEN2k, An Augmented Plane Wave + Local Orbitals Program for Calculating Crystal Properties* (Karlheinz Schwarz, Techn. Universitaet Wien, Wien, Austria, 2001).
- ¹⁹ P. Blaha, K. Schwarz, P. Sorantin, and S. B. Tricky, *Comput. Phys. Commun.* **59**, 399 (1990).
- ²⁰ J. P. Perdew, K. Burke, and M. Ernzerhof, *Phys. Rev. Lett.* **77**, 3865 (1996).
- ²¹ A. T. Zayak and P. Entel, *J. Magn. Magn. Mat.* **290-291**, 874 (2005).
- ²² A. T. Zayak, P. Entel, K. M. Rabe, W. A. Adeagbo, and M. Acet, *Phys. Rev. B* **72**, 054113 (2005).
- ²³ H. Padamsee, J. E. Neighbor, and C. A. Shiffman, *J. Low Temp. Phys.* **12**, 387 (1973).
- ²⁴ B. Mühlischlegel, *Z. Phys.* **155**, 313 (1959).
- ²⁵ N. R. Werthamer, E. Helfand, and P. Hohenberg, *Phys. Rev.* **147**, 295 (1966).
- ²⁶ A. M. Clogston, *Phys. Rev. Lett.* **9**, 266 (1962).
- ²⁷ W. L. McMillan, *Phys. Rev.* **167**, 331 (1968).
- ²⁸ M. A. S. Boff, G. L. F. Fraga, D. E. Brandao, A. A. Gomes, and T. A. Grandi, *Phys. Stat. Sol.* (a) **154**, 549 (1996).
- ²⁹ W. Lin and A. J. Freeman, *Phys. Rev. B* **45**, 61 (1991).
- ³⁰ M. A. S. Boff, G. L. F. Fraga, D. E. Brandao, and A. A. Gomes, *J. Mag. Magn. Mat.* **153**, 135 (1996).
- ³¹ F. da Rocha, G. Fraga, D. Brandao, C. da Silva, and A. Gomes, *Physica B* **269**, 154 (1999).

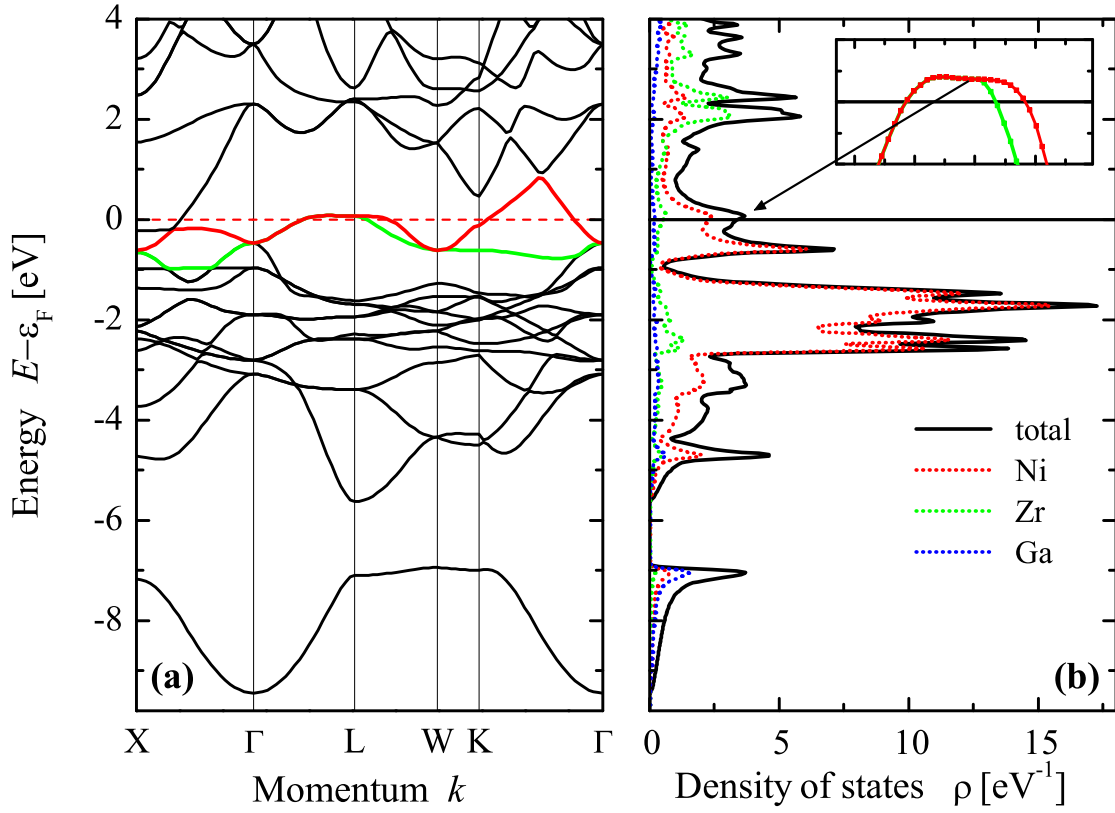


FIG. 1: Electronic structure of ZrNi_2Ga . (a) displays the band structure and (b) the density of states. The inset in (b) shows the dispersion of the bands that cause the van Hove singularity at the L -point on an enlarged scale.

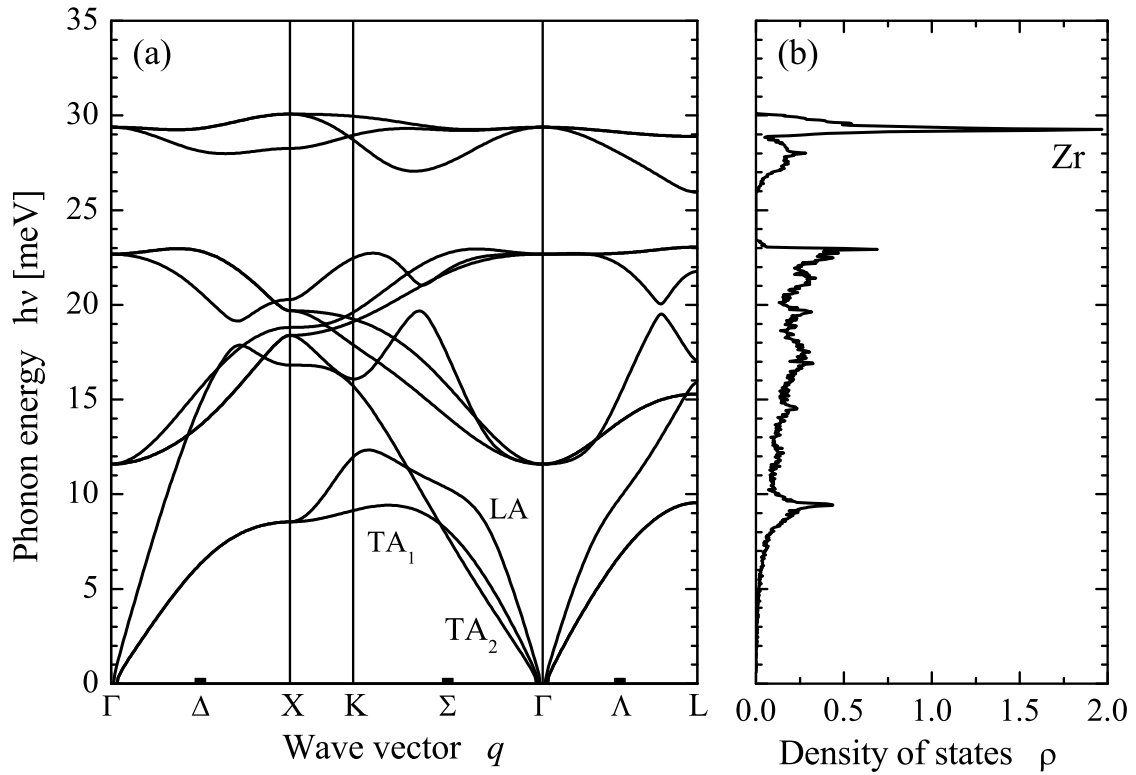


FIG. 2: The calculated vibrational spectrum of $ZrNi_2Ga$. (a) displays the phonon dispersion and (b) the corresponding density of states.

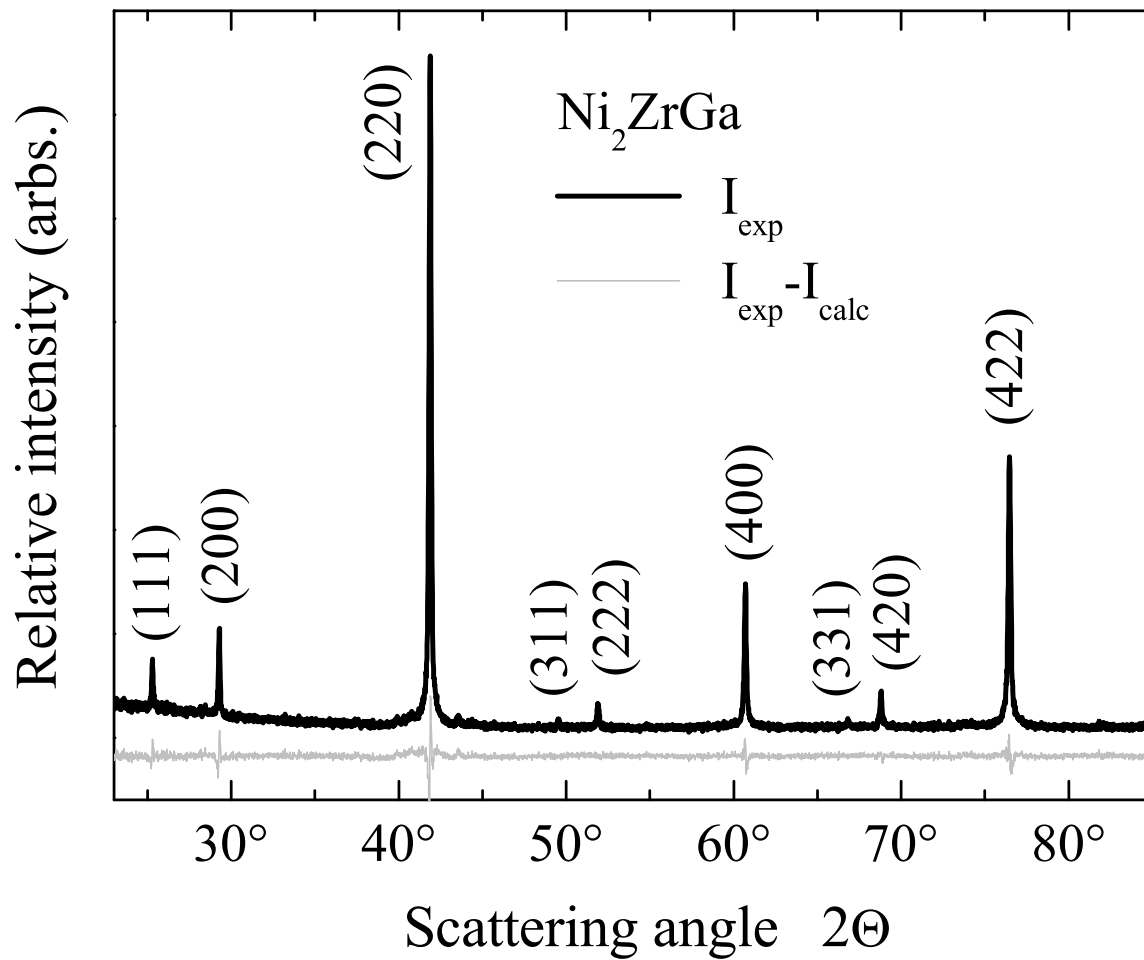


FIG. 3: Powder X-ray diffraction of ZrNi_2Ga at 300 K (black). The difference curve (grey) shows the difference between the observed data and the Rietveld refinement.

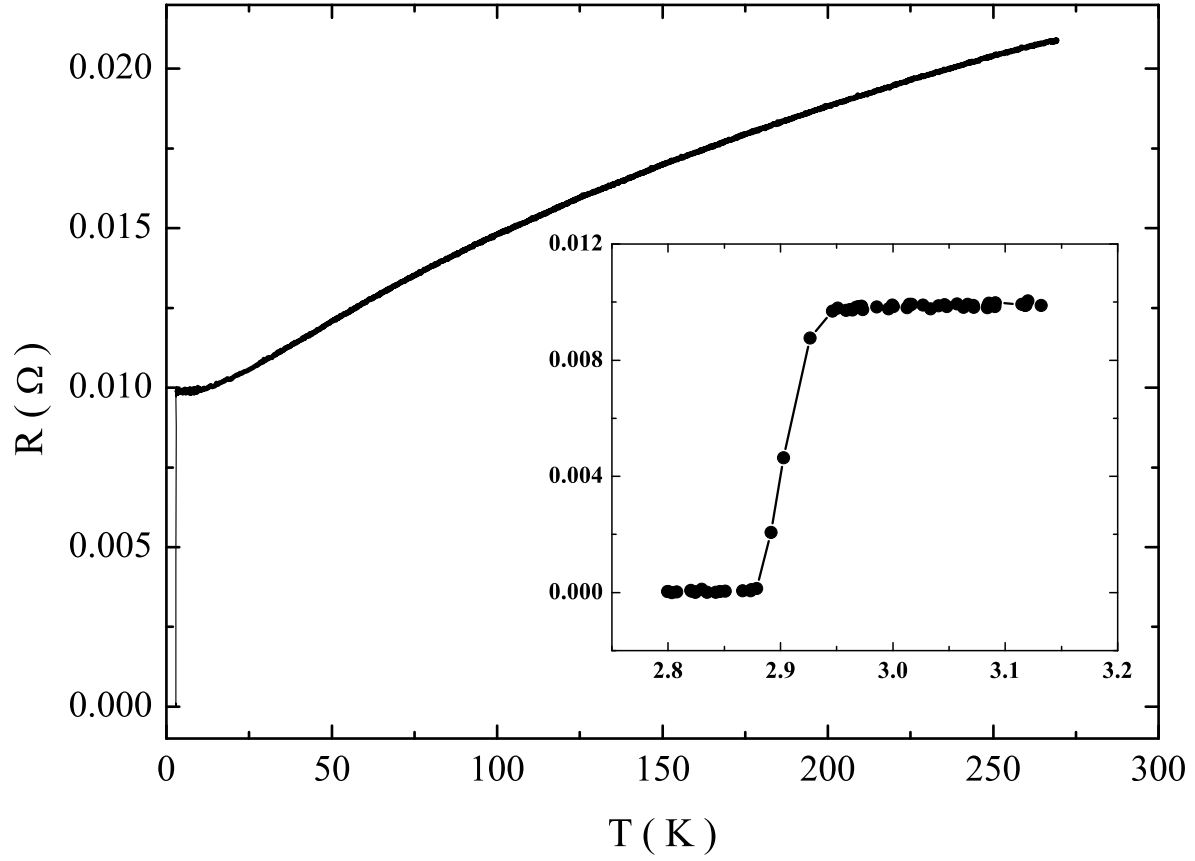


FIG. 4: The resistance of ZrNi_2Ga as a function of temperature. The inset shows an enlargement of the superconduction transition at $T_c^{mid} = 2.87$ K.

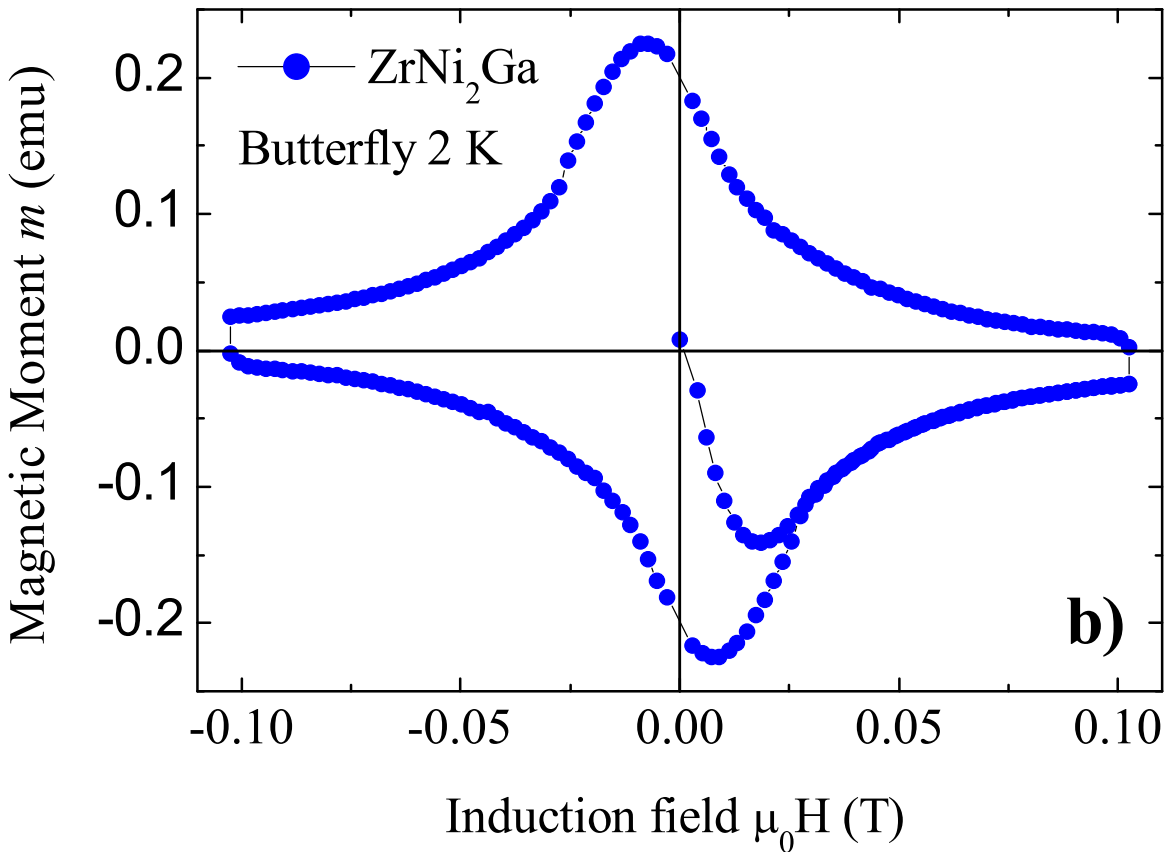
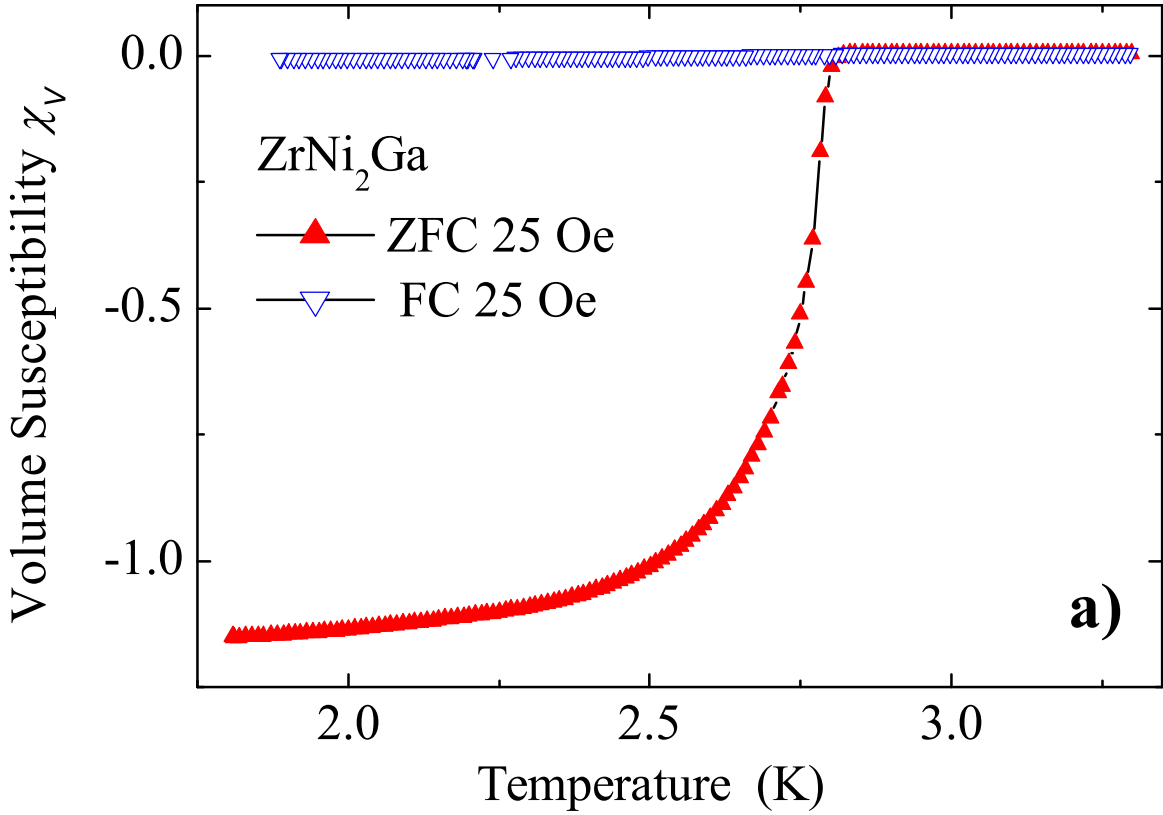


FIG. 5: (Online in color) Magnetization measurements in the superconducting state of ZrNi_2Ga .

Panel (a) shows the temperature dependent magnetization under ZFC and FC conditions. Panel

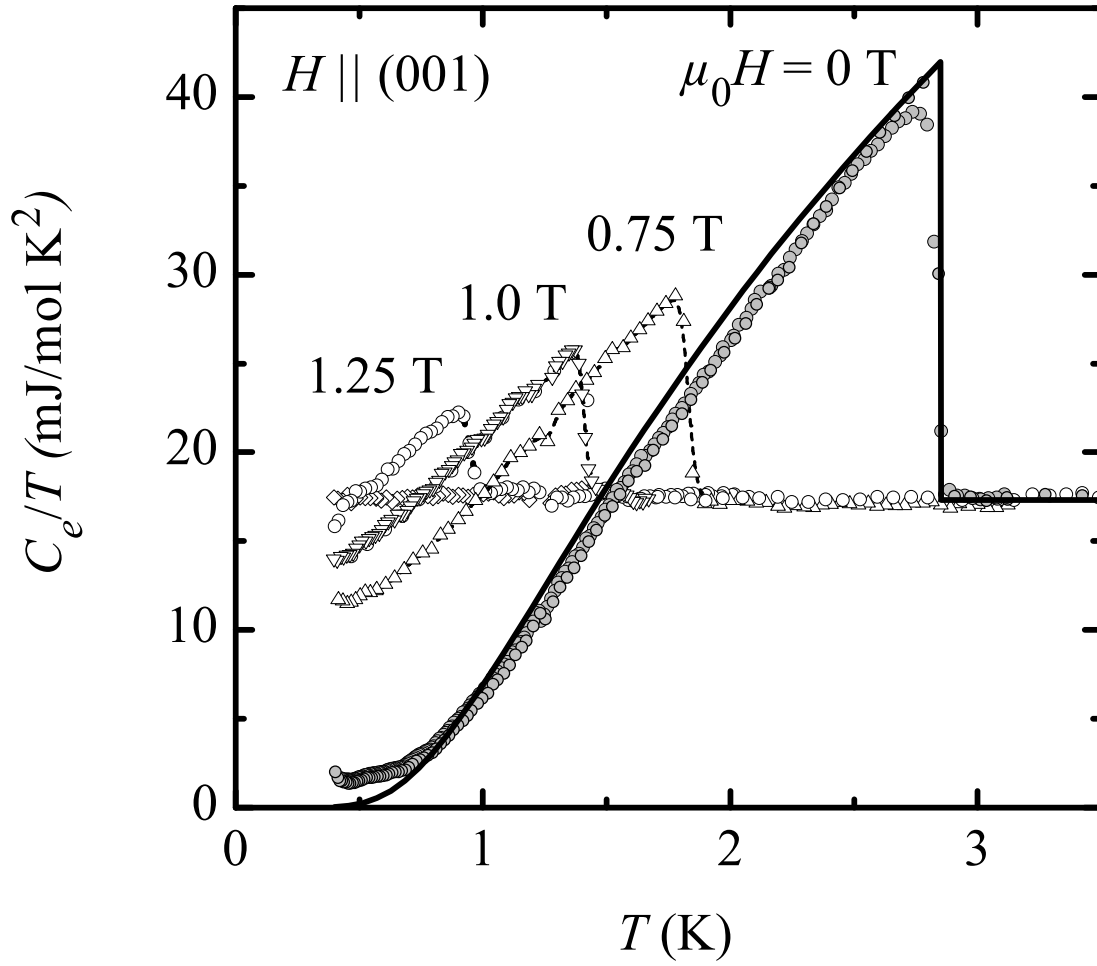


FIG. 6: Electronic contribution to the specific heat of ZrNi_2Ga divided by temperature T at various magnetic fields. The continuous line represents the calculated behavior of a weak-coupling BCS superconductor at zero magnetic field.

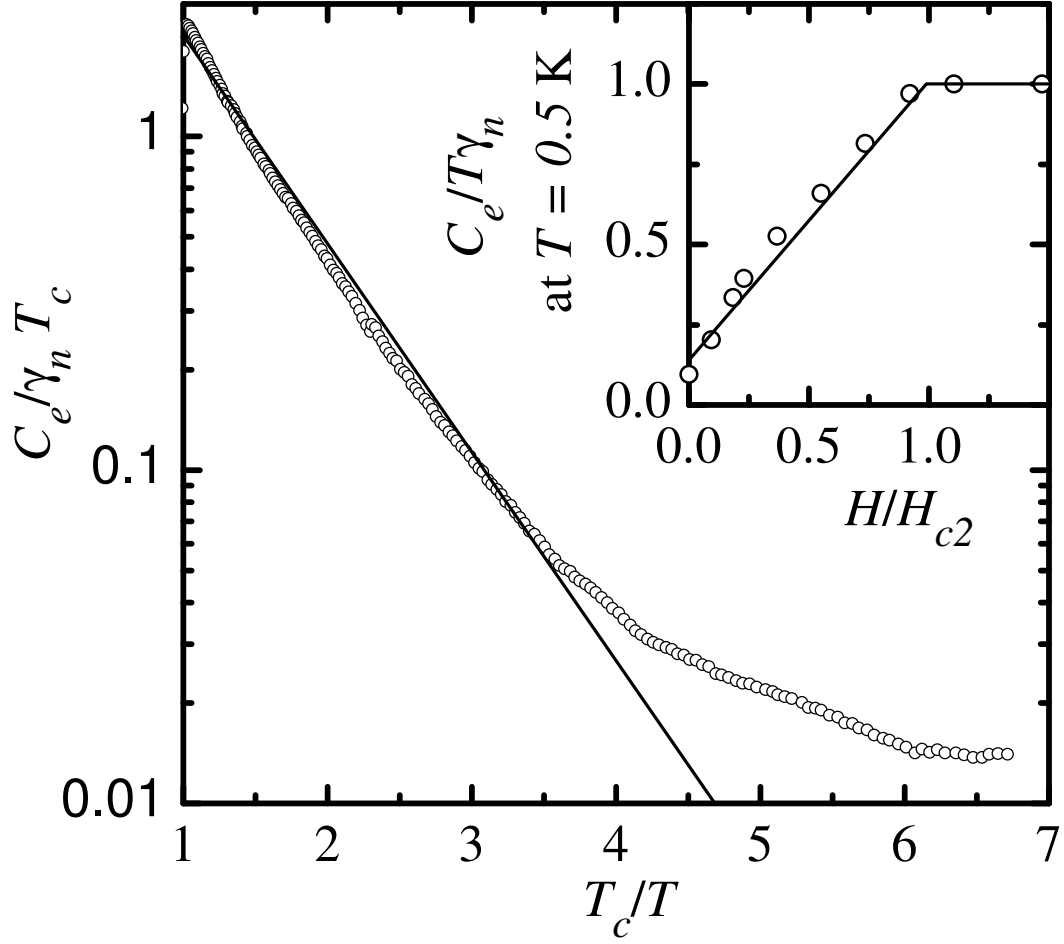


FIG. 7: Electronic contribution to the specific heat of ZrNi₂Ga at zero field divided by $\gamma_n T_c / T$ vs. T_c / T . The inset shows C_e / T at $T = 0.5$ versus the magnetic field.

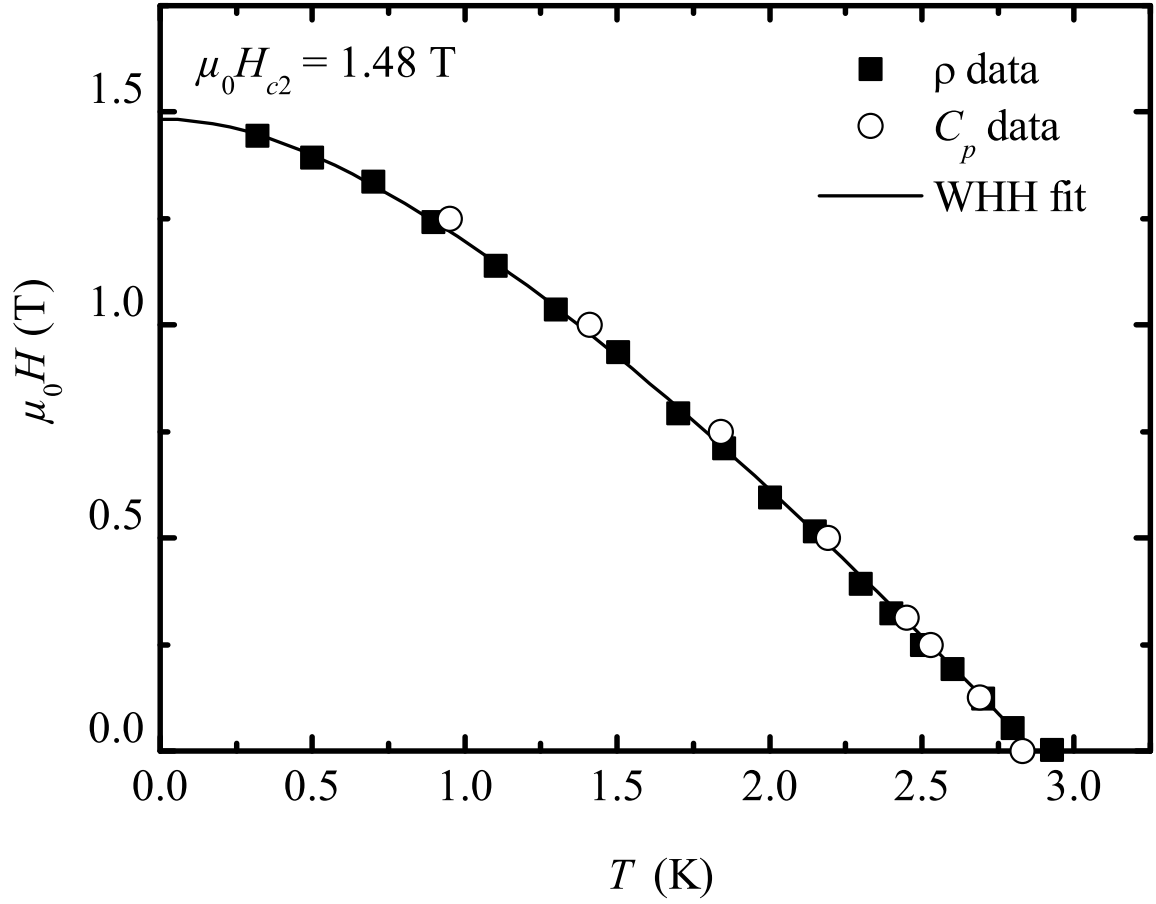


FIG. 8: Temperature dependence of the upper critical field H_{c2} of ZrNi_2Ga . Shown is a summary of the resistance and specific-heat measurements. The continuous line represents a calculation of the WHH model with $\alpha = 0$ and $\lambda_{so} = 0$, which is identical to a finite α and $\lambda_{so} \rightarrow \infty$.

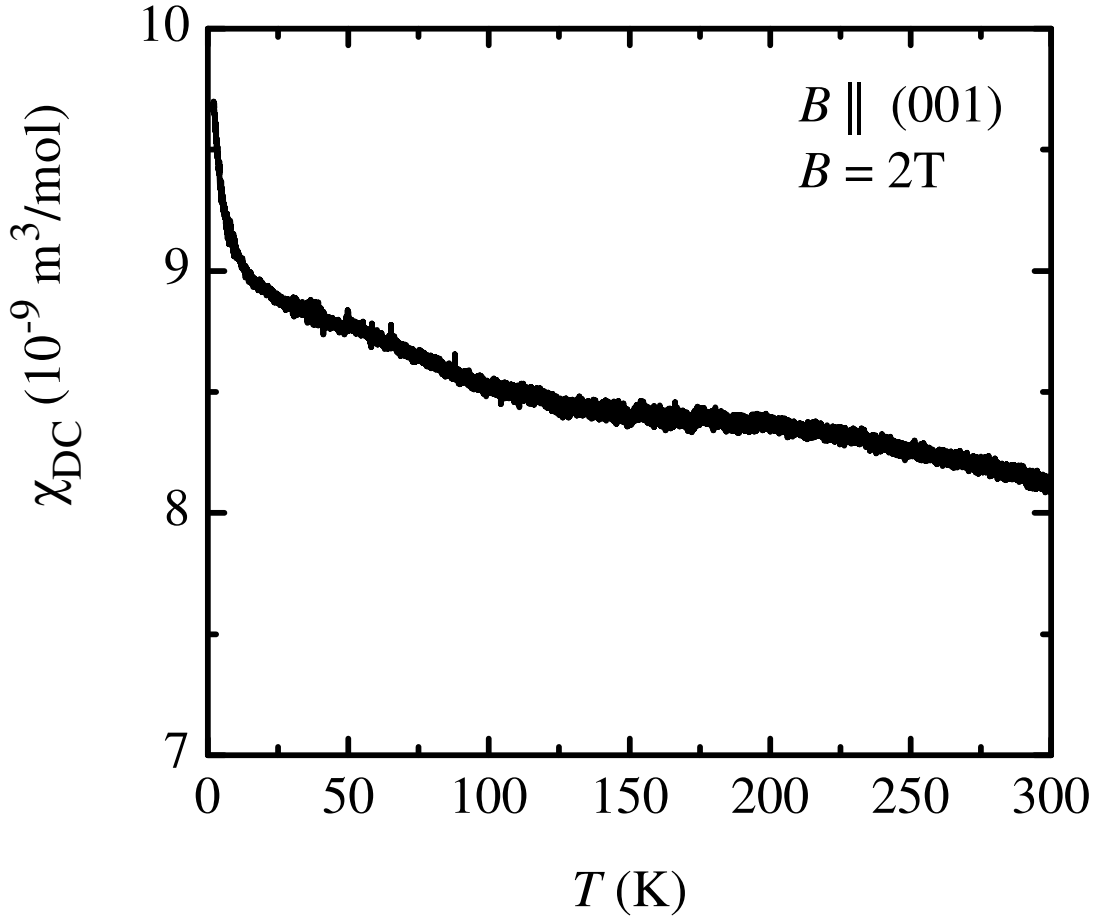


FIG. 9: Susceptibility $\chi_{DC} = M/H$ of ZrNi_2Ga in a magnetic field of $\mu_0 H = 2 \text{ T} > \mu_0 H_{c2}$. The susceptibility of the normal state shows Pauli-like behavior without any indications of magnetic order. At low temperatures there is a small Curie-Weiss-like upturn, which may be attributed to sample inhomogeneities or impurities.

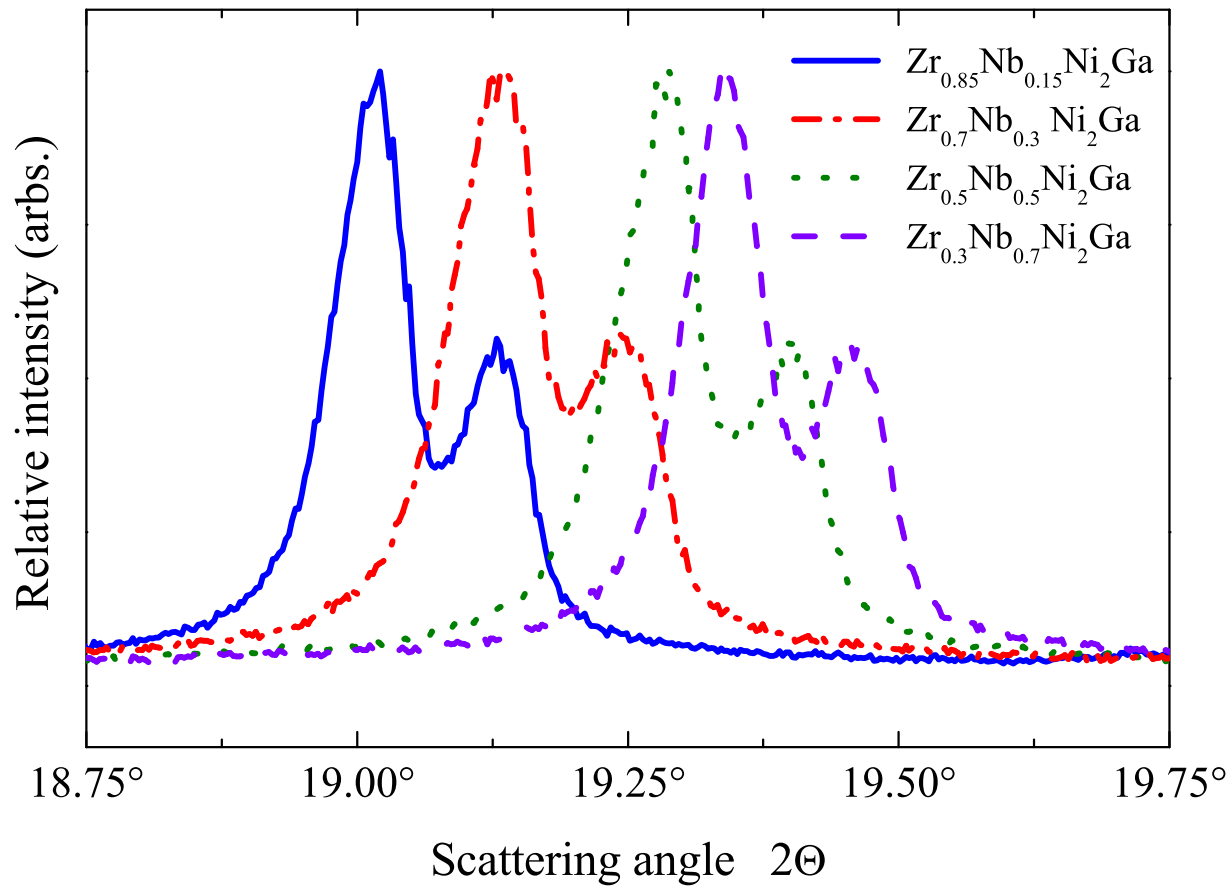


FIG. 10: Powder X-ray diffraction of the alloys $\text{Zr}_{1-x}\text{Nb}_x\text{Ni}_2\text{Ga}$ at 300 K. Shown is the region around the (220) reflection, which determines the cubic lattice parameter. The signals are splitted in Mo $K_{\alpha 1}$ and Mo $K_{\alpha 2}$ peaks.

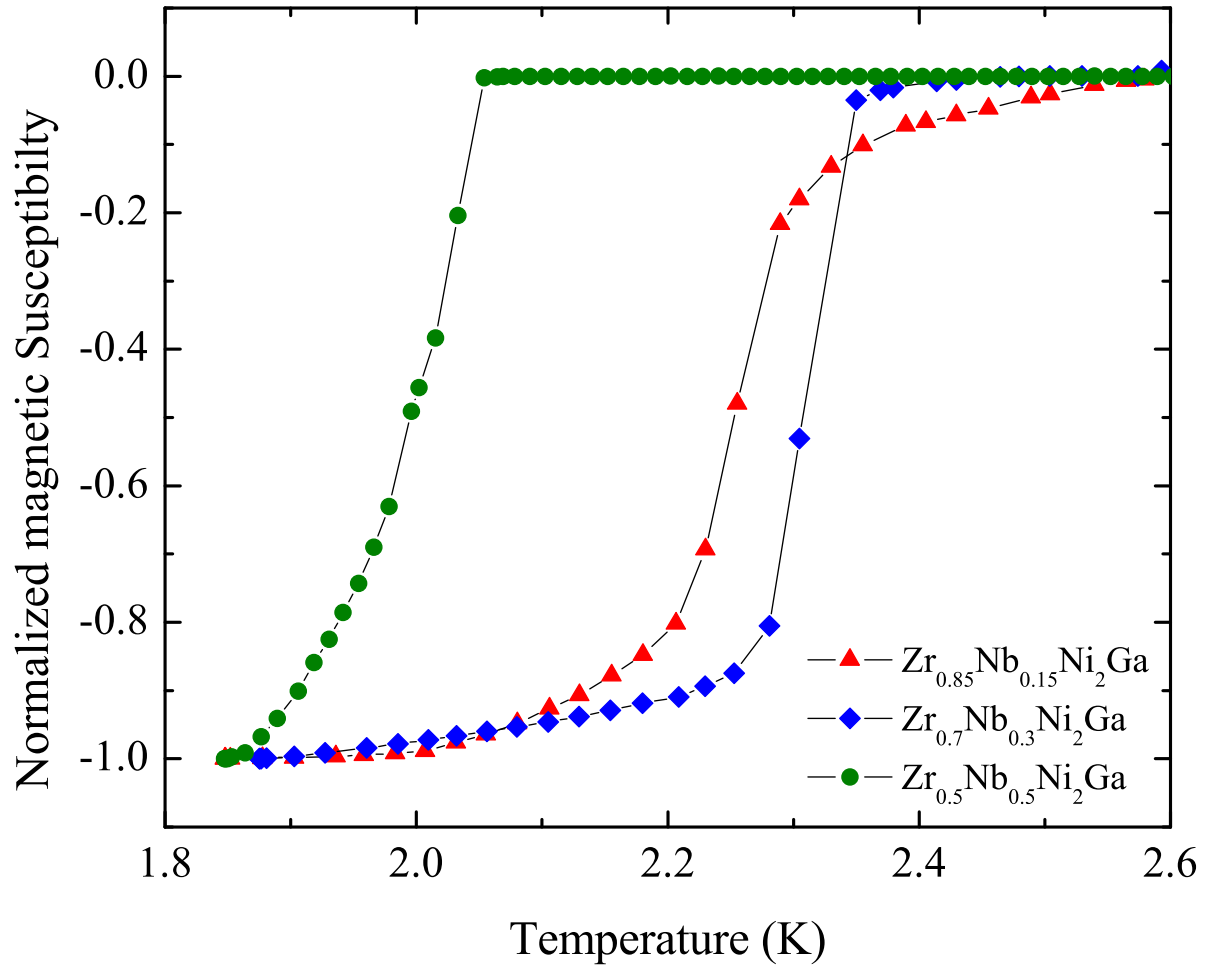


FIG. 11: (Online in color) Superconducting transitions of the alloys $\text{Zr}_{1-x}\text{Nb}_x\text{Ni}_2\text{Ga}$ under ZFC conditions. The measurements were performed with magnetic fields of $\mu_0 H = 2.5$ mT, respectively.

TABLE I: Comparison of nickel-based paramagnetic and superconducting Heusler compounds. Sommerfeld coefficient γ_n , Debye temperature Θ_D , superconducting transition temperature T_c , orbital limit of the upper critical field $\mu_0 H_{c2}^*(0) = -0.69 \cdot \mu_0 dH_{c2}/dT|_{T=T_c}$, and critical field $H_{c2}(0)$ extrapolated from low-temperature measurements.

	γ_n (mJ/mol K ²)	Θ_D (K)	T_c (K)	$\mu_0 H_{c2}^*$ (T)	$\mu_0 H_{c2}$ (T)
ZrNi ₂ Ga	17.3	300	2.85	1.48	1.48
TiNi ₂ Al	13.37 ^c	411 ^c	-	-	-
TiNi ₂ Sn	6.86 ^d	290 ^d	-	-	-
ZrNi ₂ Al	13.67 ^c	276 ^c	-	-	-
ZrNi ₂ Sn	8.36 ^d	318 ^d	-	-	-
HfNi ₂ Al	10.85 ^c	287 ^c	-	-	-
HfNi ₂ Sn	6.37 ^d	280 ^d	-	-	-
VNi ₂ Al	14.17 ^c	358 ^c	-	-	-
NbNi ₂ Al	8.00 ^a , 10.95 ^c	280 ^a , 300 ^c	2.15 ^a	0.96 ^b	> 0.70 ^a
NbNi ₂ Ga	6.50 ^a	240 ^a	1.54 ^a	0.67 ^b	~ 0.60 ^a
NbNi ₂ Sn	4.0 ^a , 5.15 ^c	206 ^a , 208 ^c	2.90 ^a , 3.40 ^c	0.78 ^b	~ 0.63 ^a
TaNi ₂ Al	10.01 ^c	299 ^c	-	-	-

^aRef. 7

^bcalculated with the initial slope dH_{c2}/dT from Ref. 7

^cRef. 31

^dRef. 28

TABLE II: Properties of the alloys $\text{Zr}_{1-x}\text{Nb}_x\text{Ni}_2\text{Ga}$ compared to ZrNi_2Ga . a are the measured lattice parameters, T_c the critical temperatures from the ZFC curves in the magnetization measurements.

Compound/Alloy	a (Å)	T_c (K)
ZrNi_2Ga	6.098	2.8
$\text{Zr}_{0.85}\text{Nb}_{0.15}\text{Ni}_2\text{Ga}$	6.074	2.4
$\text{Zr}_{0.7}\text{Nb}_{0.3}\text{Ni}_2\text{Ga}$	6.037	2.3
$\text{Zr}_{0.5}\text{Nb}_{0.5}\text{Ni}_2\text{Ga}$	5.990	2.0
$\text{Zr}_{0.3}\text{Nb}_{0.7}\text{Ni}_2\text{Ga}$	5.972	-